Article

Fat inclusions strongly alter membrane mechanics

Alexandre Santinho,[1] Aymeric Chorlay,[1] Lionel Foret,[1] and Abdou Rachid Thiam[1,*]
[1]Laboratoire de Physique de l'École Normale Supérieure, ENS, Université PSL, CNRS, Sorbonne Université, Université de Paris, Paris, France

ABSTRACT   Neutral lipids (NLs) are apolar oil molecules synthesized in the endoplasmic reticulum bilayer upon diverse biological stimuli. NLs synthesized are released in the hydrophobic core of the bilayer. At a critical concentration, NLs condense by phase separation and nucleate a lipid droplet (LD). After an LD forms, a fraction of NLs can be present in the bilayer but at a concentration below that of the nucleation. Here, we study whether and how the accumulation of NLs alters a lipid bilayer's mechanical properties. In synthetic systems, we found that NLs proffer unusual bilayer stretching capacities, especially in the presence of negatively curved phospholipids. This impact becomes spectacular when an LD is contiguous with the bilayer and supplies it with NLs. The tested NLs markedly decrease the bilayer area expansion modulus and significantly increase lysis tension but had opposite effects on membrane bending rigidity. Our data unveil how NL molecules modify overall membrane mechanics, the alteration of which may be linked to pathologies or anticancer treatments targeting NLs.

SIGNIFICANCE   Unlike phospholipids, neutral lipids (NLs) are nonsurfactants, apolar fat, or oil molecules. They are synthesized in the endoplasmic reticulum (ER) bilayer and diffuse within the bilayer's hydrophobic region. At a critical concentration, the NLs phase separate within the bilayer to form an organelle called a lipid droplet (LD). However, even if they condense into LDs, a fraction of NLs remains in the bilayer. Also, under diverse pathological conditions associated with alterations in the ER structure or composition, NLs accumulate in the membrane, failing to condense efficiently into LDs. Their removal is crucial to preserve the multiple ER bilayer functions that rely on membrane mechanics. Here, we are interested in understanding how the presence of NLs impacts such mechanics.

INTRODUCTION

Organisms from protists to humans store excess energy in carbon-rich molecules that are often neutral lipids (NLs) (1,2). NLs are apolar fat molecules, different from phospholipids, which are the building blocks of cellular membranes. The most abundant NLs are triacylglycerols, which are structurally the closest NL to phospholipids, and sterol esters, which are most closely related to cholesterol, another membrane constituent (3). However, other NLs are found depending on cell type and metabolic condition, such as retinyl ester, phytyl esters, squalene, acylceramides, etc. (2,4–7). Most of these NLs are synthesized in the bilayer of the endoplasmic reticulum (ER) (8,9). Because of their hydrophobicity, NLs accumulate within the bilayer's hydrophobic region as dissolved and mobile hydrophobic inclusions (10). When their concentration reaches a critical

value, NLs phase separate within the bilayer and nucleate an oil lens (11,12), which grows and buds off to become an independent organelle called a lipid droplet (LD) (8). In the context of nucleation phenomena, the formation of an LD consists of packaging a large fraction of the NLs into a condensed phase, in equilibrium with a dilute NL phase in the bilayer (7,11).

Avoiding the accumulation of NLs in the ER membrane ensures its proper functioning. NL accumulation could increase the bilayer's thickness, which would likely cause membrane stresses and affect the stability of transmembrane proteins. Indeed, such an accumulation may alter membrane structure, fluidity, lipid distribution, and stability, which can cause various forms of membrane stress. Most of these disturbances can explain the onset of diseases or cell death when NL molecules accumulate in the ER bilayer and are not properly removed and packaged into LDs.

The assembly of triacylglycerol LDs is facilitated by membrane curvature, composition, and specific proteins (10,13–18) that decrease the critical nucleation concentration (10,19–21). Accordingly, when the ER's curved structure is lost because of the dysfunction in the ER shaping

proteins, triacylglycerols accumulate in the bilayer, unable to effectively condense into LDs (10,18). These conditions are associated with several diseases, such as spastic paraplegia (22). Other factors, like the ER membrane phospholipid composition and surface tension, can also regulate the concentration of the bilayer-dissolved NLs (14) and their propensity to condense into LDs (23). Likewise, the NL chemistry determines its tendency to remain in the bilayer or condense into an LD (10,14). Squalene, an intermediate molecule in the synthesis of sterols, is an example of NL that abnormally accumulates in membranes (6,14,24). Increasing the proportion of squalene relative to triacylglycerols leads to the formation of larger LDs (14), probably because squalene increases the nucleation concentration (6,24) and decreases the budding propensity of LDs (14). Interestingly, many anticancer and antifungal drugs target the squalene epoxidase (25–27), leading to reduced cellular cholesterol and, inevitably, an accumulation of squalene. These two consequences may concomitantly contribute to cellular death.

In this work, we ask the fundamental question of how NL molecules, referred to as fat or oil molecules hereafter, modulate the mechanical properties of a phospholipid bilayer. To answer this question, we used model membranes based on the formation of giant unilamellar vesicles (GUVs) containing neutral lipids, such as those from droplet-embedded vesicles (28,29) or inverted emulsion vesicles (30). We found that oil molecules' presence substantially modifies the bilayer response to stretching and bending, depending on the phospholipid composition and oil type.

MATERIALS AND METHODS

All experiments were performed in the following HKM buffer: 50 mM Hepes, 120 mM potassium acetate, and 1 mM $MgCl_2$ (in Milli-Q water) at pH 7.4 and 280 ± 15 mOsm.

Preparation of GUVs

GUVs were prepared by electroformation. Phospholipids and mixtures thereof in chloroform at 0.5 μM were dried on an indium tin oxide-coated glass plate. The lipid film was desiccated for 1 h. The chamber was sealed with another indium tin oxide-coated glass plate. The lipids were then rehydrated with a sucrose solution (280 ± 15 mOsm). Electroformation was performed using 100 Hz AC voltage at 1.0–1.4 Vpp and maintained for at least 2 h. This low voltage was used to avoid hydrolysis of water and dissolution of the titanium ions on the glass plate. GUVs were either stored in the chamber at 4°C overnight or directly collected with a Pasteur pipette.

GUV composition for used phospholipid mixtures

1,2-dioleyl-sn-3glycero-3-phosphocholine (PC) GUVs were 100% PC, 1,2-dioleoyl-sn-glycero-3-phosphoethanolamine (PE)-PC GUVs were 50% PE and 50% PC, 1,2-dioleoyl-sn-glycero-3-phosphate (PA)-PC GUVs were 30% PA and 70% PC, 1,2-dipalmitoyl-sn-glycero-3-phosphocholine (DPPC)-PC GUVs were 40% DPPC and 60% PC, and 1-stearoyl-2-arachidonoyl-sn-glycero-3-phosphocholine (PufaPC)-PC GUVs were 30% PufaPC and 70% PC.

Preparation of DEVs

To prepare the oil droplets, 5 μL of the oil (triolein or squalene) was added to 70 μL of HKM buffer. The mixture was sonicated. The diameter of the resulting droplets is on the order of a few hundred nanometers. To make droplet-embedded vesicles (DEV), GUVs were then incubated with the LDs for 5 min. To make DEVs with triolein-NBD (1,3-Di(cis-9-octadecenoyl-2-((6-(7-notrobenz-2-oxa-1, 3-diazol-4-yl) amino) hexanoyl), the oil was composed of 99.95% of triolein and 0.05% (w/w) of To-NBD. The GUV-LD mixture was then placed on a glass coverslip (pretreated with 10% (w/w) bovine serum albumin (BSA) and washed three times with buffer) and observed with a confocal microscope.

Preparation of GUVs by the inverted emulsion technique

Two phospholipid mixtures were diluted in chloroform at 0.5 μM and dried. A 150 μL oil volume was poured onto one mixture and 200 μL of HKM buffer onto the other one. These solutions were sonicated for 5 min to facilitate the solubilization of phospholipids. A 100 μL volume of the oil-phospholipid mixture was deposited on the HKM-phospholipids solution. Then, the remaining 50 μL of the oil-phospholipid mixture was mixed with 4 μL of an HKM-sucrose 1:1 (w/w) solution to generate a water-in-oil inverted microemulsion, which was then added to the HKM-contacting-oil solution. The resulting mixture was centrifuged for 3 min. The oil-containing GUVs were next collected in the aqueous volume.

Confocal microscope images

All micrographs of DEVs were made on a Carl ZEISS LSM 800 (Carl Zeiss, Oberkochen, Germany) with a 63× oil immersion objective or 10× air objective, and observed samples were held by glass coverslips (24 × 36 mm #0; Menzel Gläser, Saarbrückener, Germany).

Hypotonic shock

DEVs were produced following the techniques described above. The resulting solution was placed on a coverslip (pretreated with 10% (w/w) BSA and washed three times with buffer) and observed with a confocal microscope (10× objective). Spherical DEVs with no thermal fluctuation of the bilayer have been selected so that the surface of the bilayer can be easily determined. Next, 50 μL of Milli-Q water was added to 120 μL of DEV solution to apply an osmotic shock of $\Delta C = 80$ mOsm. The osmotic gradients applied were always the same ($\Delta C = 80$ mOsm for Figs. 1, 2, and 3 and S1–S3) except for Figs. 1, D and E and S1, J–M, because of permeability protocol precautions, where the ΔC was 145 mOsm, and for Figs. 2 B and S2 A to report rapid triolein partitioning, where ΔC was 210 mOsm. The DEVs were then imaged overtime to follow the evolution during swelling. The same protocol was used to apply hypotonic shock to GUVs or oil-containing-GUVs (Figs. 1 F, 2 D, and 3, D–F).

Determination of the critical bilayer strain

The maximal expansion of the bilayer is given by the following equation:

$$\varepsilon_{max} = \frac{A_{max} - A_0}{A_0},$$

where A_{max} and A_0 are the maximal areas of the bilayer before burst (stretched state) and the area before starting the swelling experiments (unstretched state), respectively. This area was determined by fitting a circle onto the DEV (GUV) bilayer and recording its radius. The radius of the embedded droplets was also recorded for DEV swelling experiments to
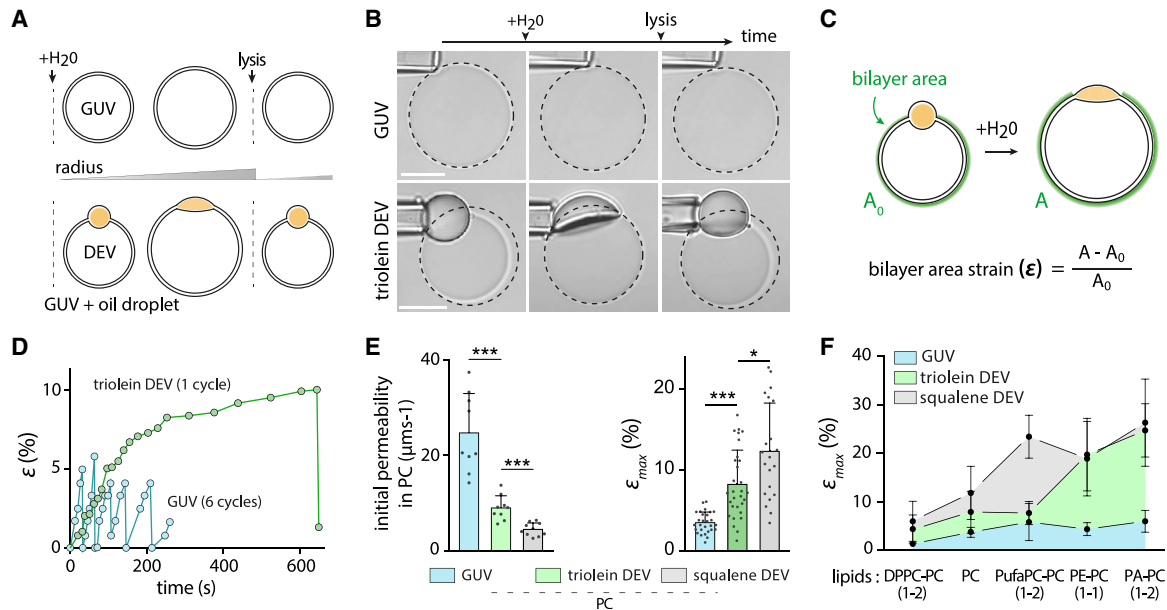
FIGURE 1 Oil droplets connected to a bilayer expand the critical membrane area strain. (*A*) Top: schematic representation of the behavior of a GUV under hypotonic shock is given. GUVs undergo swelling and burst cycles. Bottom: schematic representation of a triolein DEV (droplet-embedded vesicle) system compared with a GUV, which also undergoes swelling and burst cycles. (*B*) Time lapse of triolein DEV and GUV during a hypotonic shock experiment. Black dashed circles report maximal vesicle radius. Scale bars, 10 μm. (*C*) Top: green arc underlying the bilayer area for uninflated and inflated DEV is shown. Bottom: formula used to compute the bilayer strain, ε, defined as the relative expansion of the bilayer area. (*D*) Corresponding bilayer strain ε variations of triolein DEVs and GUVs over time of Fig. 1 *B* are shown. Swelling and burst cycles are clearly visible for GUVs (*blue dots*; six cycles) and DEVs (*green dots*; one cycle). (*E*) Left: plot of the initial water permeability of PC bilayer of GUVs (n = 8), triolein DEVs (n = 9), and squalene DEVs (n = 9). Mean ± SD. Right: plot of the critical bilayer strain (ε_{max}) of GUVs (*blue*, n = 28), triolein DEVs (*green*, n = 29), and squalene DEVs (*gray*, n = 21) for PC bilayer. Mean ± SD. (*F*) Plot of the critical bilayer strain (ε_{max}) of GUVs (*blue*), triolein DEVs (*green*), and squalene DEVs (*gray*) for various phospholipid compositions of the bilayer. Mean ± SD. ***p < 0.001; **p < 0.01; *p < 0.05. To see this figure in color, go online.

determine the corrected surface area of the DEV bilayer (see the section below).

Bilayer surface area of the DEVs

To consider only the surface of the DEV's bilayer, the surface occupied by the embedded droplet had to be removed. To do this, we calculated the surface of the sphere formed by the bilayer and subtracted the surface of the spherical cap corresponding to the droplet (Fig. S1 *C*). This gave the following expression of the surface area of the DEV bilayer (A)

$$A_{DEV} = 2\pi R_g^2 \times \left(1 + \sqrt{1 - \left(\frac{R_d}{R_g}\right)^2} \right),$$

where R_g and R_d are the DEV radius and droplet radius, respectively.

Permeability assay

To determine permeability, we made osmotic shock experiments thanks to an applied osmotic gradient between the outside and inside of the vesicles of $\Delta C = 145$ mOsm. To do so, we added 20 μL of DEVs (or GUVs) sucrose solution (280 ± 15 mOsm) into 100 μL HKM buffer. Then, we added 100 μL of Milli-Q water to induce an osmotic shock. During the experiment, we maintained the DEVs (or the GUVs) thanks micropipettes, to have a clear determination of both vesicle radius and droplet radius (see Fig. 1 *C* and Supporting materials and methods). This enables to determine the permeation area and the volume of the vesicle as a function of time during the swelling experiment.

GUVs, triolein DEVs, and squalene DEVs initial permeability computation

See Supporting materials and methods for the computation of the initial permeability.

Determination of the triolein concentration in the bilayer

To determine the concentration of triolein molecules in the bilayer, we used triolein DEVs (or triolein GUVs). The triolein mixture was made of 99.95% triolein and 0.05% (w/w) of triolein-NBD. For all our experimental conditions involving these measurements (Figs. 1, 2, and 3), we chose DEVs (triolein GUVs) with a radius between 5 and 15 μm with micrometric triolein droplets. DEV snaps were taken by keeping the same settings for each DEV. Then, fluorescence profiles were drawn perpendicular to the bilayer of triolein DEVs (or triolein GUVs) and averaged over 15 pixels. The maximal value of the profiles was recorded and averaged over multiple DEVs. The same protocol was used for Cy5-PE fluorescence signals measurements (Fig. 3 *C*). For monitoring of triolein concentration in the bilayer (Fig. S1, *D* and *E*), we captured images every 5 min to avoid bleaching of the triolein-NBD signal.

FRAP experiment: triolein-NBD bleaching in the bilayer

Fluorescence recovery after photobleaching (FRAP) experiments were performed by bleaching a part of the DEV bilayer (Fig. S1, *B* and *C*). The To-NBD signal was bleached; then, the fluorescence signal recovery was
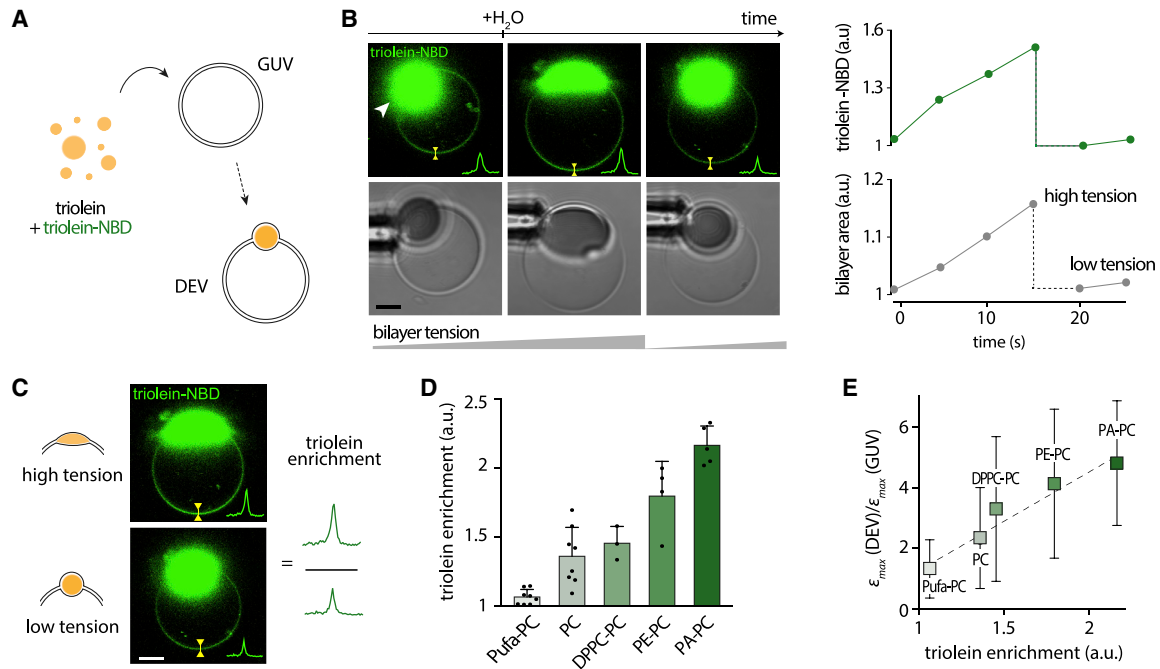
FIGURE 2   Stretching increases the oil concentration in the bilayer depending on the phospholipid composition. (A) Schematic representation of the triolein DEV formation protocol. To report triolein distribution, triolein was supplemented with 0.05% (w/w) triolein-NBD. (B) Left shows confocal images of PC triolein DEVs under hypotonic shock with triolein tagged by triolein-NBD. Line scans show a triolein-NBD signal colocalizing with the bilayer. Scale bars, 5 μm. Right shows corresponding quantification of triolein-NBD signal and bilayer area variation. During bilayer stretching, triolein-NBD signal increased and quickly dropped after deflation. (C) Representative confocal fluorescence images of a PC triolein DEV at the maximal bilayer expansion state (high tension) and at the "unstretched" state (low tension). Line scans allow for quantification of triolein-NBD fluorescence intensity in the bilayer in each state. "Triolein enrichment" was computed by taking the fluorescence ratio between stretched state/unstretched state. Scale bars, 5 μm. (D) Triolein enrichment measured for PC (n = 8), PA-PC (n = 5), PE-PC (n = 4), DPPC-PC (n = 3), and PufaPC-PC (n = 8) triolein DEVs. Mean $\pm$ SD. (E) Plot of the critical bilayer strain ratio between DEVs/GUVs against the triolein enrichment for previous phospholipid compositions. Statistical analysis revealed a significant slope different from zero for a linear fit (dotted lines). Mean $\pm$ SD. ***p < 0.001; **p < 0.01; *p < 0.05. To see this figure in color, go online.

monitored. The FRAP curve is normalized by the fluorescence before bleaching DEVs and just after the bleach (in nonbleached regions). GraphPad Prism was used to fit the FRAP recovery curve with a nonlinear regression and the exponential "one-phase association model."

BODIPY fluorescence in squalene DEVs during hypotonic shock

To follow BODIPY fluorescence signal during hypotonic shock upon squalene DEVs (Fig. S2 F), 0.5 μL of BODIPY was added in 100 μL of HKM buffer containing squalene DEVs. After 10 min, 20 μL of water was added to the coverslip, and the evolution of BODIPY signal in the bilayer of the squalene DEV was monitored.

Micromanipulation and surface tension measurements by micropipette-aspiration-applied bilayer tension

Micropipettes were made from capillaries drawn out with a Sutter Instruments (Novato, CA) pipette puller. They were used to manipulate GUVs, DEVs, or GUVs containing oil. The pipettes were incubated for 30 min in a 5% BSA solution before use, to prevent droplets and membranes from adhering to the glass.

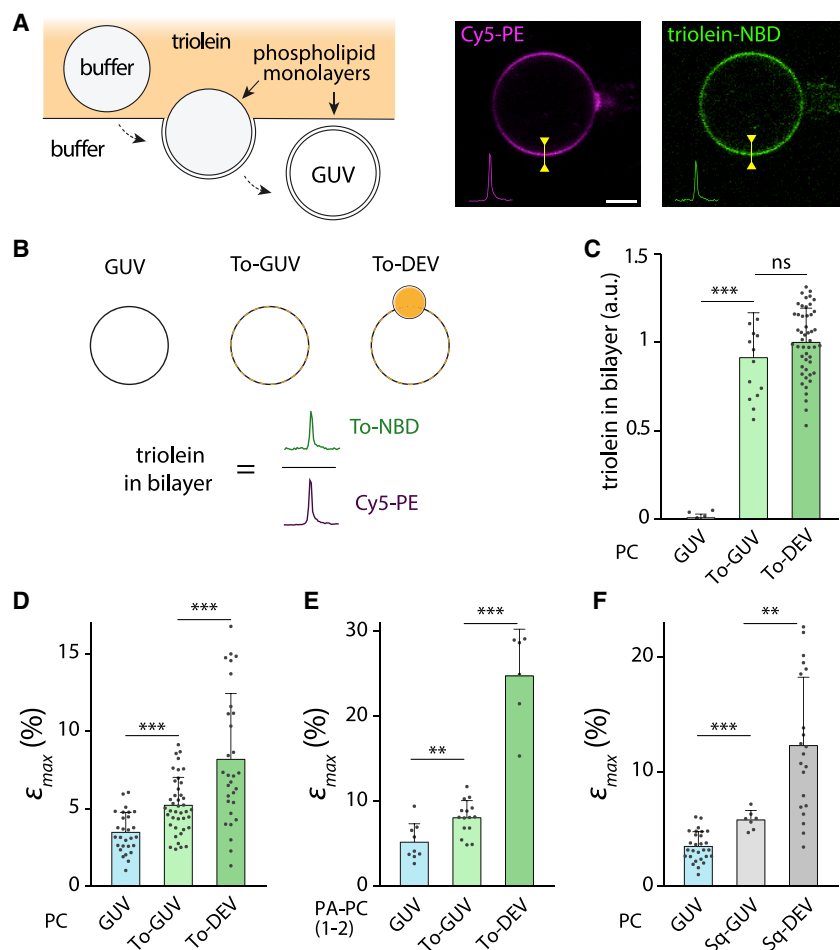Additionally, surface tensions of bilayers were measured using the same pipettes. Using Laplace's law and measuring the pipette inner radius, the GUV radius, and suction pressure, the surface tension of the bilayer can be determined by

$$\gamma = \frac{\Delta P_{suc}}{2\left(\frac{1}{R_p} - \frac{1}{R_g}\right)},$$

where ΔP_{suc}, R_p, and R_g are the suction pressure, the pipette inner radius, and the vesicle radius, respectively.

The suction was carried out using a syringe. The resulting pressure was measured with a pressure transducer (DP103; Validyne Engineering, Northridge, CA), the output voltage of which was monitored with a digital voltmeter. The pressure transducer (range 55 kPa) was calibrated before the experiments. Micropipettes were made from capillaries (1.0 oD × 0.58 iD × 150 Lmm 30-0017 GC100-15b; Harvard Apparatus, Holliston, MA) with a micropipette puller (model P-2000; Sutter Instruments). Micromanipulation (TransferMan 4r) was provided by Eppendorf (Hamburg, Germany).

For bending rigidity measurements (see Bending rigidity measurements) that needed a better measurement precision, the suction was applied thanks to a water reservoir whose height was controlled with a micrometer gauge (precision 0.005 mm). The resulting suction pressure was determined by measuring the water level variation.

Lysis tension measurements

To determine an estimation of the bilayer lysis tension of GUVs, DEVs, or GUVs containing oil, we used the micropipette aspiration technique.

FIGURE 3 The sole presence of oil molecules increases the critical bilayer strain. (*A*) Left, illustration of the formation of triolein GUVs (To-GUVs) using a water-in-oil inverted emulsion method. The triolein was tagged with 0.05% (w/w) of triolein-NBD. Right, fluorescence confocal imaging of the resulting triolein GUVs. Significant triolein-NBD signal colocalizes with the bilayer reported by Cy5-PE. Scale bars, 5 μm. (*B*) Top shows three different model systems: a bilayer with no neutral lipids (GUV), a bilayer supplemented with triolein molecules (To-GUVs), and a bilayer supplemented with triolein molecules provide by a triolein droplet (To-DEVs). Bottom: to assess the concentration of triolein in the bilayer of the three model systems, we compute the "triolein in bilayer" by taking the fluorescence ratio between triolein-NBD signal/Cy5-PE signal; microscope settings were kept constant. (*C*) Quantification of the triolein in bilayer for GUVs (n = 6), triolein GUVs (n = 13), and triolein DEVs (n = 49) made with PC phospholipids is given. Mean $\pm$ SD. *t*-test shows no significant difference of triolein in bilayer between triolein GUVs and triolein DEVs. (*D*) Quantification of the critical bilayer strain (ε_{max}) of PC GUVs (n = 28), triolein GUVs (n = 41), and triolein DEVs (n = 29), showing higher stretching for DEVs and GUVs containing oil. Mean $\pm$ SD. (*E*) Plot of the critical bilayer strain (ε_{max}) for PC-PA GUVs (n = 9), triolein GUVs (n = 15), and triolein DEVs (n = 6) showing higher stretching for DEVs and GUVs containing oil. Mean $\pm$ SD. (*F*) Quantification of the critical bilayer strain (ε_{max}) of PC GUVs (n = 28), squalene GUVs (Sq-GUV) (n = 7), and squalene DEVs (Sq-DEVs) (n = 21), showing higher stretching for DEVs and GUVs containing oil. Mean $\pm$ SD. ***p < 0.001; **p < 0.01; *p < 0.05. To see this figure in color, go online.

Thanks to a slight aspiration, a bilayer tongue was sucked into the micropipette. The aspiration was then increased at an approximate rate of 2–3 mbar/s, causing a proportional increase in the bilayer surface tension (see Micromanipulation and surface tension measurements by micropipette-aspiration-applied bilayer tension). At a certain tension, the bilayer ruptured because of a pore opening. The measured lysis tension was taken as the higher tension reached just before bilayer rupture.

Bending rigidity measurements

First, streptavidin-coated microspheres were added to the bulk on the glass coverslip. Then, the GUV was gently captured by one of the two micropipettes to control the surface tension γ. One streptavidin-coated microsphere was caught by the other micropipette, and it was slowly moved toward the GUV. Upon contact, the biotinylated phospholipid of the GUV interacted strongly with the streptavidin-coated microsphere surface. Finally, a nanotube was pulled by removing slowly the micropipette in the opposite direction as the GUV.

The bending rigidity was obtained with the following equation:

$$R_t = \sqrt{\frac{\kappa}{2\gamma}},$$

where κ is the bending rigidity of the membrane that has to be determined with the experimental measurements of the bilayer tension γ (see Microma-nipulation and surface tension measurements by micropipette-aspiration-applied bilayer tension) and nanotube radius R_t.

To obtain R_t, we vary the tube length at a constant displacement velocity of 2.5 μm $\cdot$ s^{-1} at constant surface tension, which keeps the radius constant based on the previous equation. Therefore, for a given tension, we have many couples of tube length L_t and tongue length L_p in the micropipette. The conservation of surface yields

$$L_p = \delta \times L_t + b$$

Thus, from this conservation, the slope (δ) was extracted by measuring different couples of L_p and L_t. We also checked that we do not detect hysteresis on these curves (Fig. S4, *H* and *I*) to ensure that we reached equilibrium for the oil partitioning (for triolein GUVs and squalene GUVs) between the nanotube and the GUV.

On the other hand, conservation of the volume of the system links the radius of the tube to that of the GUV (R_g) and the pipette through the following equation (31):

$$R_t = \delta \times \left(1 - \frac{R_p}{R_g}\right) \times R_p$$

Finally, different values of R_t, associated with a different value of γ were measured, which gave us a mean value for κ with the first equation of this section.

Apparent area expansion modulus measurements

GUVs or oil-containing GUVs were gently captured with a micropipette. Then, aspiration in the micropipette was slowly increased to obtain multiple values of membrane tension (~20 s between each point). For each value of micropipette aspiration (MPA)-applied bilayer tension, the variation of the length of the bilayer tongue in the micropipette and the radius of the GUV were measured, allowing us to determine an approximate variation at the first order of the surface area of the bilayer of the GUV ΔA (32):

$$\Delta A = 2\pi R_p \left(1 - R_p \left/ R_g \right. \right)\Delta L_p,$$

where ΔL_p, R_p, and R_g are the variation of the bilayer tongue length in the micropipette, the pipette inner radius, and the GUV radius, respectively.

The MPA-applied bilayer tension was then plotted against the relative surface area variation of the GUV's bilayer. Because the GUV was already slightly tensed (initial tension above 0.1 mN/m), the membrane fluctuation is negligible, and the MPA-applied bilayer tension (γ) can be linked to the surface area variation ($\Delta A/A_0$) by the apparent area expansion modulus (Y):

$$Y_{app} = \frac{\gamma}{\Delta A/A_0}$$

Therefore, the slope of the MPA-applied bilayer tension-surface area variation curve gave the apparent area expansion modulus of the membrane (Y_{app}).

Area expansion modulus computing

Area expansion modulus was determined following the experiment in the Apparent area expansion modulus measurements and previously determined bending rigidity κ. To plot the MPA-applied bilayer tension γ against the relative surface area variation $\Delta A/A_0$ as above, the MPA-applied bilayer tension is the plot as a function of

$$\frac{\Delta A}{A_0} + \Delta \alpha$$

with

$$\Delta \alpha = -\left(K_B T \left/ 8\pi\kappa \right.\right)\ln(\gamma \left/ \gamma_0 \right.)$$

K_B is the Boltzmann constant, T the room temperature in Kelvin, and γ_0 the initial MPA-applied bilayer tension at the beginning of the experiment. Therefore, the slope of the MPA-applied bilayer tension- $(\Delta A /A_0)+ \Delta \alpha$ curve gave the area expansion modulus (Y) (32).

Quantification and statistical analysis

Statistical analysis

The statistical comparison was made using a Student parametric test in which we assume a Gaussian distribution. Then, the test is an unpaired t-test. The statistical analyses were made with GraphPad Prism 7.0a; *** indicates $p < 0.001$, ** indicates $p < 0.01$, and * indicates $p < 0.05$.

When the bar graph is plotted, values shown in the text and figures are mean $\pm$ standard deviation (SD). When only the data set of one experiment is shown, the values on the graph are absolute value $\pm$ uncertainty of measurements.

Equipment and reagents

Equipment

All micrographs were made on a Carl ZEISS LSM 800. Glass coverslips were from Menzel Gläser (24 × 36 mm #0). Micropipettes were made from capillaries (1.0 OD × 0.58 ID × 150 Lmm 30-0017 GC100-15b; Harvard Apparatus) with a micropipette puller (model P-2000; Sutter Instruments). Micromanipulation was performed with TransferMan 4r (Eppendorf). Pressure measurement unit (DP103) was provided by Validyne Engineering.

Chemical products

Phospholipids: PC, PE, PA, DPPC, PufaPC 18:0–20:4, biotynil-PE (1,2-dioleyl-sn-glycero-3-phosphoethanolamine-N-(biotinyl)), Rh-PE (1,2-dioleyl-sn-glycero-3-phosphoethanolamine-N-lissamine rhodamine B sulfonyl), and Cy5-PE (1,2-dioleoyl-sn-glycero-3-phosphoethanol-amine-N-(Cyanine 5)) were from Avanti Polar Lipids (Alabaster, AL). BODIPY 493/503 was from Thermo Fisher Scientific (Waltham, MA). Triolein and squalene were from Sigma-Aldrich (St. Louis, MO), and To-NBD glycerol was from Setareh Biotech (Eugene OR). Streptavidin-coated microspheres were from Bangs Laboratories (Fishers, IN). Hepes (54457–250-F), potassium acetate (P1190), MgCl2 (M8266-100G), BSA 98% (A7906-100G), and sucrose 99.5% (59378-500G) were from Sigma-Aldrich.

RESULTS

Oil droplets expand the critical bilayer area strain while decreasing permeability

We opted for osmotic swelling as a straightforward mean to probe the expansion capacity of a GUV bilayer (Fig. 1 A, top; (33–36)). To investigate whether NLs alter this expansion, we used the DEV system (37), consisting of a GUV containing an oil droplet made of triolein, the major triacylglycerol NL (Fig. 1 A, bottom). In the DEV system, the oil droplet equilibrates within seconds, with a constant fraction of triolein molecules mobile in the bilayer (Fig. S1, A–E; (10)).

We prepared GUVs and triolein oil-based DEVs (Fig. 1 B, bottom), both made of 1,2-dioleoyl-sn-glycero-3-phospho-choline (DOPC) phospholipid, and we subjected them to the same osmotic shock. Both systems showed swelling and bursting cycles during which their bilayer underwent stretching and relaxation phases (Fig. 1, A and B; (33)). To describe and understand the systems' response, we focused on the bilayer surface area strain ε for both GUVs and DEVs (Fig. 1 C). For DEVs, the bilayer area is calculated at each time point by withdrawing the space occupied by the droplet from the area of the sphere fitting the bilayer (Fig. 1 C; Fig. S1, F–I). Furthermore, the DEVs' swelling time took a few minutes (Fig. 1, C and D), much longer than the time it takes for triolein oil molecules to partition between the droplet and the bilayer (10). Therefore, the swelling process of DEVs occurred at equilibrium.

Triolein DEVs had a slower strain rate than GUVs (initial slope, Fig. 1 D), which underwent many cycles within the same time lapse. The strain rate is determined by the water

flux, i.e., the permeability of the bilayer; the higher the permeability, the higher the strain rate. Accordingly, we found a permeability higher for GUVs, $24.8 \pm 8.3 \ \mu m \cdot s^{-1}$, than triolein DEVs, $9.0 \pm 2.6 \ \mu m \cdot s^{-1}$ (Fig. 1 E, left; Fig. S1, J–M; Supporting materials and methods; (32)). Squalene DEVs were less permeable than triolein DEVs (Fig. 1 E, left; Fig. S1, J, L, and M; Supporting materials and methods), consistent with permeability studies with droplet interface bilayers (38).

The critical strain $\boldsymbol{\varepsilon}_{max}$, reached when the bilayer bursts, was higher for DEVs than GUVs (Figs. 1 D and E, right, and S1 J). A burst occurs when a critical pore size appears in the membrane. GUVs stretched at a slower strain rate have a higher probability of reaching the critical pore size (33) and therefore a lower $\boldsymbol{\varepsilon}_{max}$. This correlation is not verified with DEVs, which had slower strain rates than GUVs but higher $\boldsymbol{\varepsilon}_{max}$ (Fig. 1 D and E, right). Therefore, other factors absent in GUVs favor the increase in $\boldsymbol{\varepsilon}_{max}$ for DEVs. We hypothesized that oil molecules recruited to the bilayer are responsible for this higher critical bilayer strain for DEVs.

To test our hypothesis, we decided to vary the phospholipid composition, which controls the bilayer's oil concentration (14). We worked with different phospholipid mixtures, including DOPE (PE), DOPA (1,2-dioleoyl-sn-glycero-3-phosphate; PA), DPPC, or PufaPC (18:0, 20:4). For each condition, we determined the critical bilayer strain, $\boldsymbol{\varepsilon}_{max}$, and compared it between GUVs and DEVs (Figs. 1 F and S1, N–R). Regardless of composition, triolein DEV bilayers withstood larger expansions than GUVs (Figs. 1 F and S1 R). Interestingly, the critical bilayer strain of triolein DEVs was systematically higher in the presence of negatively curved lipids such as PA and PE, between three and five times higher than for GUVs (Figs. 1 F and S1 R). We found that squalene enabled a higher membrane expansion than triolein in PC conditions and, more strikingly, in PufaPC (Figs. 1 F and S1 R). This particular increase in PufaPC may pertain to π-π interactions between the numerous unsaturations in the squalene's carbon skeleton and those in the PufaPC acyl chain. However, compositions containing PA and PE showed no difference between the two oils (Figs. 1 F and S1 R), suggesting that these phospholipids' contribution masked the difference between the two oils.

Stretching increases the bilayer oil concentration depending on the phospholipid composition

Based on the above results, we hypothesize that the oil droplet buffers oil molecules to the bilayer, which has more material to withstand more significant expansions. Following this hypothesis, PA and PE would lead to more oil molecules in the bilayer.

To test our model, we used a fluorescently labeled "triolein," triolein-NBD, mixed with triolein at 0.05% (w/w),

to report for triolein localization (Fig. 2 A). The resulting DEV was then monitored during the osmotic swelling (Fig. 2 B, left). We found that the bilayer's triolein signal increased concomitantly with the bilayer stretching (Fig. 2 B, right). Then, the bilayer concentration sharply decreased after a rapid burst of the DEV (Fig. 2 B, right); the oil molecules almost spontaneously re-equilibrated between the droplet and the bilayer after this burst (Fig. 2 B; Fig. S2 A). These results show that increasing the bilayer surface tension by osmotic swelling raises the amount of oil in the bilayer, agreeing with previous in silico results (14) and confirmed here by using micropipettes to vary surface tension (Fig. S2, B and C). To test whether squalene behaves like triolein, we used BODIPY, which labels the bilayer's hydrophobicity, as we could not find available fluorescent squalene reporters. We observed a stronger BODIPY signal in the bilayer during osmotic swelling, most likely because of an increase in squalene in the bilayer (Fig. S2 D).

Our hypothesis suggests that the number of oil molecules incorporated into the bilayer during swelling determines the extent of membrane expansion. Because the critical bilayer strain depended on the phospholipid type (Figs. 1 F and S1 R), we measured the triolein increase in the bilayer for each phospholipid condition. We found an increase in the triolein signal during swelling for all lipid compositions but to different extents (Figs. 2 D and S2 E). We defined the bilayer triolein enrichment as the ratio between the triolein level in the bilayer at the maximal expansion (high tension) and the initially unstretched bilayer (low tension) (Fig. 2 C). We found that DEVs containing PA or PE, which had the most remarkable expansion (Fig. 1 F), displayed the highest triolein enrichment (Fig. 2 D). In contrast, triolein DEVs made with PufaPC-PC, which did not significantly increase the critical bilayer strain (Fig. 1 F), exhibited a low triolein enrichment. These data are consistent with our model: during stretching, triolein molecules can behave as membrane building blocks, like phospholipids, and allow for more bilayer expansion.

If our model is correct, then the enrichment level of triolein in the bilayer should dictate the critical bilayer strain. To test this prediction, we considered for each phospholipid composition the ratio of the critical bilayer strain of DEVs/GUVs (Fig. 1 F). This normalization cancels the contribution of phospholipids to the membrane expansion and highlights the contribution of triolein molecules. Consistent with our prediction, we found that the amount of triolein injected into the bilayer during stretching increases linearly with the critical bilayer strain ratio (Fig. 2 E).

In summary, an oil droplet connected to a bilayer equilibrates with residual oil molecules in the bilayer. The concentration of this residual oil increases as the bilayer is stretched. Phospholipids with negative spontaneous curvature favor a higher delivery of oil molecules from the droplet

to the stretched bilayer and, thereupon, a higher critical bilayer strain.

The sole presence of oil molecules in a bilayer increases the critical area strain

To fully demonstrate that the oil molecules favored the increase in the critical bilayer strain, we decided to repeat the previous experiments with oil molecules in the bilayer without any droplet reservoir. To do so, we used the water-in-oil inverted emulsion method (30) by using a triolein oil phase containing triolein-NBD (Fig. 3 A, left). With this approach, indeed, we found that the resulting GUVs, called triolein GUVs, carried only triolein molecules in their bilayer (Fig. 3 A, right). The bilayer triolein concentration is defined as the triolein-NBD bilayer signal divided by Cy5-PE, reporting phospholipids (Fig. 3 B). Based on this normalization, triolein GUVs and DEVs composed of PC and not subjected to an osmotic swelling had a similar bilayer triolein signal (Fig. 3 C).

We first compared GUVs and triolein GUVs, both made of PC, subjected to osmotic swelling. We found that the critical bilayer strain, ε_{max}, for triolein GUVs was significantly higher than for GUVs (Fig. 3 D), consolidating our model that the sole presence of NLs is sufficient to increase the membrane expansion limit.

We next compared triolein GUVs to triolein DEVs. Triolein DEVs had a 1.45-fold higher membrane expansion limit than triolein GUVs in PC (Fig. 3 D). The presence of PA exacerbated this difference by 3.2-fold higher (Figs. 3 E and S3, A and B). These observations agree with our model. Indeed, the bilayer of triolein GUVs had a fixed number of oil molecules and, therefore, less material to withstand larger expansions; in contrast, the bilayer of a triolein DEV can be continuously supplied with oil molecules by the droplet. PA highlighted further this difference because it induced the most substantial triolein release into the bilayer of DEVs (Fig. 2, D and E). Finally, squalene had a similar impact than triolein in squalene GUVs versus squalene DEVs (Fig. 3 F).

Overall, these data show that the oil molecules' presence increases the bilayer's ability to withstand more extensive stretching than a pure phospholipid membrane. If a NL droplet is physically connected to an expanding bilayer, it will buffer it with NLs and further increase its expansion. A dramatic consequence of such an increment in the bilayer stretching is that the area per phospholipid can be increased by severalfold by NLs, especially in the presence of negatively curved phospholipids (Figs. 1 F and 3, D–F).

Oil molecules modify the mechanical properties of a bilayer

We wanted to know whether the mechanical properties of the bilayer are influenced by the presence of oil, as it was observed for solvents (39). The critical bilayer surface area strain is determined by the appearance of a critical pore size, which depends on membrane stretching and bending factors (33). We probed how NLs altered these mechanical factors independently.

First, we studied whether NLs altered the lysis tension of DEVs, i.e., the surface tension at which a pore opens in the bilayer. We used micropipette suction to increase the surface tension of PC GUVs and PC DEVs made of triolein or squalene. The MPA-applied bilayer tension was increased continuously by pulling on the bilayer at a rate of ∼2–3 mbar/s (Fig. S4 A). The lysis tension was taken as the MPA-applied bilayer tension recorded right before the bilayer's burst (Fig. S4 A). In PC, the lysis tension of GUVs was 8.1 ± 1.9 mN/m, in the range of previously reported values (32,40). Triolein increased this lysis tension to 9.7 ± 1.9 mN/m, and squalene DEVs led to a more significant increase to 10.8 ± 2.2 mN/m (Fig. 4 A). A similar trend was found for a PC-PA membrane composition (Fig. S4 B). This increase in the lysis tension can partly explain the higher critical bilayer area strain proffered by oil molecules (Figs. 1 F and S1 R).

Secondly, we determined the impact of the oil molecules on the area expansion modulus. For surface tensions over 0.5 mN/m, sufficient to smoothen thermal membrane fluctuations, the apparent area expansion modulus is given by Hooke's law (Fig. 4 B; (41,42)). Experimentally, we increased the bilayer area with a micropipette while recording its MPA-applied surface tension (Fig. 4 B). The slope of the resulting MPA-applied bilayer tension-area curve (Fig. S4, C and D) yields the apparent area expansion modulus of the bilayer (Y_{app}) (42). With this approach, we could only work with GUVs containing oils (Fig. 3 A) because, in DEVs, the droplet has a contribution in elasticity difficult to model. GUVs made of PC had an apparent expansion area modulus of 194 ± 25 mN/m (41), whereas those bearing triolein and squalene had lower values, 89 ± 31 and 111 ± 27 mN/m, respectively (Fig. 4 C). This marked decrease in the apparent area expansion modulus is consistent with the overall increase in the critical bilayer strain observed when the NL oils are present in the bilayer (Fig. 3, D and E). However, no significant difference was found between squalene and triolein, suggesting that the apparent area expansion modulus does not solely account for the disparity in the critical bilayer strain between these two oils (Fig. 1 F).

Finally, we determined the bending rigidity (K) by nanotube pulling experiments (Figs. 4 D and S4, E–I). We found that the presence of triolein in a PC GUV bilayer decreased the bending rigidity (12 ± 4 k_BT) roughly by a factor of two compared with the value for a bare GUV (21 ± 4 k_BT) (Fig. 4 E); a similar trend was found when measuring the rigidity by fluctuation analysis (43). Surprisingly, squalene slightly increased the bending rigidity (27 ± 4 k_BT), illustrating that oil molecules do not necessarily change
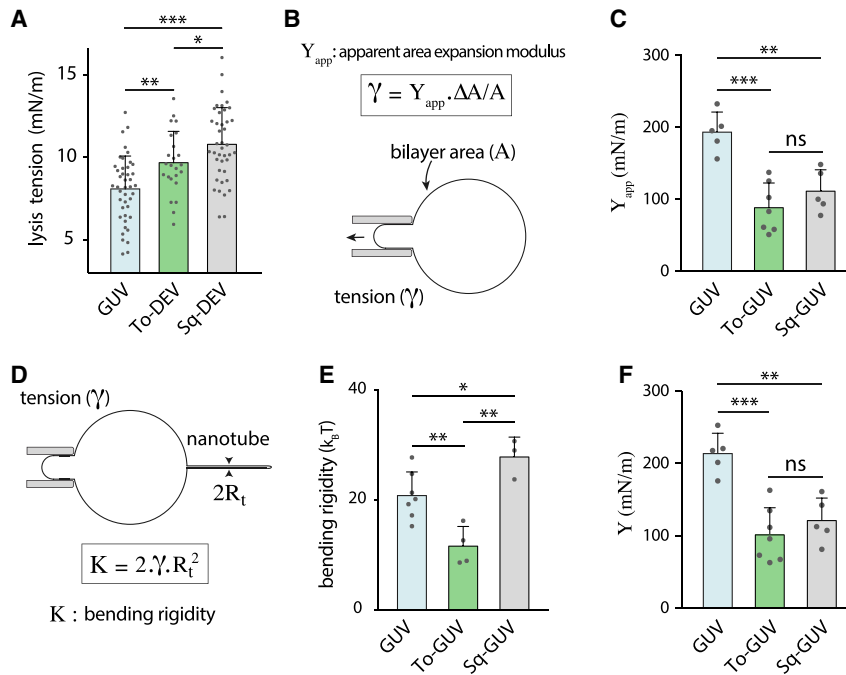
membrane properties in the same way. We used the bending rigidity values to compute the absolute area expansion moduli (Y) (Fig. 4 *F*; (32)). PC GUVs had an expansion area modulus of 214 ± 25 mN/m (41), whereas GUVs containing triolein or squalene had a lower value of 101 ± 35 and 120 ± 28 mN/m (Fig. 4 *F*).

In conclusion, the above data illustrate how and which membrane mechanical properties are altered by NL oil molecules. NLs can have similar or opposite effects on membrane mechanical properties, depending on the NLs' chemistry.

DISCUSSION

Precise control of the biophysical properties of membranes is crucial for cell survival. Phospholipids and membrane proteins often control these properties. Here, we consider the impact of neutral lipids, which can behave as hydrophobic membrane inclusions. We found that neutral lipids proffer unusual mechanical properties to the bilayer membrane. Such an effect depends on the nature of the hydrophobic inclusion but also the phospholipid composition.

We worked with triolein, the main component of cellular LDs, and squalene, which can significantly accumulate in cells upon drug treatments targeting the squalene epoxidase (25–27). For the phospholipid conditions that we tested, we found that these neutral lipids increased the lysis tension of a bilayer and significantly decreased its area expansion modulus. Whereas triolein decreased the bilayer bending stiffness, squalene increased it. Overall, these mechanical

alterations are consistent with the greater membrane expansion proffered by the neutral lipids. At the molecular level, the increased critical membrane strain likely results from the insertion of neutral lipids between phospholipids when the membrane is stretched, i.e., when tension increases. Thus, the neutral lipids may adopt different molecular conformations when tension varies (44–46). At low tension, triolein molecules could remain perpendicular to the phospholipids but parallel to them at high tension, exposing their glycerol backbone to water (45). This molecular adaptability would allow phospholipids to be spaced further apart than in a pure bilayer.

Squalene is a long terpene with numerous unsaturation, chemically different from triolein. Despite contrasting chemistry, the two neutral lipids yielded similar elasticity. As for triolein, squalene may also adopt phospholipid-parallel or antiparallel orientations in the bilayer (47), depending on the surface tension, in a way that decreases the area expansion modulus. Concerning the membrane lysis tension, both neutral lipids increased it, especially squalene. This difference may pertain to the interaction spectrum of NLs with phospholipids. In particular, squalene can develop multiple interactions π-π (48) with phospholipids, making it act like a molecular glue, "cross-linking" the bilayer leaflets and delaying the opening of a pore.

Interestingly, squalene increased the bilayer bending rigidity, whereas triolein decreased it, relative to GUVs.

The bending rigidity (κ) depends on the bilayer thickness (*d*), the area expansion modulus (*Y*), and the coupling constant (β) of the monolayer leaflets composing the

bilayer: $\kappa \propto \beta \times d^2 \times Y$ (49). Triolein and squalene decreased the area expansion modulus, Y (Fig. 4 F), by two, which tends to reduce the bending rigidity, but not for squalene (Fig. 4 E). Squalene particularly increases membrane thickness, more than triacylglycerols (38,39,50,51). Also, via π-π interactions developed with phospholipids (48), squalene likely increases the monolayer coupling β. Consequently, the contribution of $\beta \cdot d^2$ for squalene may compensate for the decrease in Y sufficiently to overall increase the bending rigidity κ.

Based on the above analysis and the rigidity measurement (Fig. 4 E), curving squalene-rich membranes is more difficult. Squalene accumulation is promoted by several antifungal and anticancer drugs (25–27), and therefore, the subsequent alteration in membrane mechanics could contribute to the death of fungal or cancer cells. Inducing the synthesis and membrane accumulation of specific neutral lipids could be a strategy to prompt cancer cells to die.

Finally, our data show that a droplet connected to a bilayer can supply neutral lipids to the membrane, especially when the bilayer experiences stretching. The amount of neutral lipids delivered to the bilayer depends on the bilayer phospholipid composition. Thus, in a cellular context, LDs should be disconnected from the ER bilayer to avoid residual neutral lipids in the membrane. If not, the neutral lipid accumulation would hinder the ER's multiple functions that rely on the precise regulation of its mechanical properties, involving membrane tubulation, stretching, budding, or fusion.

In conclusion, our study provides important insights into how neutral lipids can change membranes' biophysical properties. This study is relevant to better understand the ER membrane mechanics during fat storage, particularly in pathological conditions in which neutral lipids fail to efficiently phase separate into LDs. Our approaches can be adapted to test the behavior of more exotic lipids.

SUPPORTING MATERIAL

AUTHOR CONTRIBUTIONS

A.R.T. designed research. A.C. and A.S. performed experiments and analyzed the data with L.F. A.C., A.S., and A.R.T. wrote the manuscript.

ACKNOWLEDGMENTS

REFERENCES

1. Murphy, D. J., and J. Vance. 1999. Mechanisms of lipid-body formation. *Trends Biochem. Sci.* 24:109–115.

2. van Wijk, K. J., and F. Kessler. 2017. Plastoglobuli: plastid microcompartments with integrated functions in metabolism, plastid developmental transitions, and environmental adaptation. *Annu. Rev. Plant Biol.* 68:253–289.

3. Walther, T. C., and R. V. Farese, Jr. 2012. Lipid droplets and cellular lipid metabolism. *Annu. Rev. Biochem.* 81:687–714.

4. Ajat, M., M. Molenaar, …, J. B. Helms. 2017. Hepatic stellate cells retain the capacity to synthesize retinyl esters and to store neutral lipids in small lipid droplets in the absence of LRAT. *Biochim. Biophys. Acta Mol. Cell Biol. Lipids.* 1862:176–187.

5. Senkal, C. E., M. F. Salama, …, L. M. Obeid. 2017. Ceramide is metabolized to acylceramide and stored in lipid droplets. *Cell Metab.* 25:686–697.

6. Spanova, M., T. Czabany, …, G. Daum. 2010. Effect of lipid particle biogenesis on the subcellular distribution of squalene in the yeast *Saccharomyces cerevisiae*. *J. Biol. Chem.* 285:6127–6133.

7. Thiam, A. R., and E. Ikonen. 2021. Lipid droplet nucleation. *Trends Cell Biol.* 31:108–118, Published online December 5, 2020.

8. Olzmann, J. A., and P. Carvalho. 2019. Dynamics and functions of lipid droplets. *Nat. Rev. Mol. Cell Biol.* 20:137–155, Pblished online December 6, 2018.

9. Pol, A., S. P. Gross, and R. G. Parton. 2014. Review: biogenesis of the multifunctional lipid droplet: lipids, proteins, and sites. *J. Cell Biol.* 204:635–646.

10. Santinho, A., V. T. Salo, …, A. R. Thiam. 2020. Membrane curvature catalyzes lipid droplet assembly. *Curr. Biol.* 30:2481–2494.e6.

11. Thiam, A. R., and L. Forêt. 2016. The physics of lipid droplet nucleation, growth and budding. *Biochim. Biophys. Acta.* 1861:715–722.

12. Khandelia, H., L. Duelund, …, J. H. Ipsen. 2010. Triglyceride blisters in lipid bilayers: implications for lipid droplet biogenesis and the mobile lipid signal in cancer cell membranes. *PLoS One.* 5:e12811.

13. Adeyo, O., P. J. Horn, …, J. M. Goodman. 2011. The yeast lipin orthologue Pah1p is important for biogenesis of lipid droplets. *J. Cell Biol.* 192:1043–1055.

14. Ben M'barek, K., D. Ajjaji, …, A. R. Thiam. 2017. ER membrane phospholipids and surface tension control cellular lipid droplet formation. *Dev. Cell.* 41:591–604.e7.

15. Choudhary, V., O. El Atab, …, R. Schneiter. 2020. Seipin and Nem1 establish discrete ER subdomains to initiate yeast lipid droplet biogenesis. *J. Cell Biol.* 219:e201910177.

16. Joshi, A. S., B. Nebenfuehr, …, W. A. Prinz. 2018. Lipid droplet and peroxisome biogenesis occur at the same ER subdomains. *Nat. Commun.* 9:2940.

17. Kassan, A., A. Herms, …, A. Pol. 2013. Acyl-CoA synthetase 3 promotes lipid droplet biogenesis in ER microdomains. *J. Cell Biol.* 203:985–1001.

18. Wang, S., F.-Z. Idrissi, …, P. Carvalho. 2018. Seipin and the membrane-shaping protein Pex30 cooperate in organelle budding from the endoplasmic reticulum. *Nat. Commun.* 9:2939.

19. Chung, J., X. Wu, …, R. V. Farese, Jr. 2019. LDAF1 and seipin form a lipid droplet assembly complex. *Dev. Cell.* 51:551–563.e7.

20. Zoni, V., W. Shinoda, and S. Vanni. 2020. Seipin accumulates and traps diacylglycerols and triglycerides in its ring-like structure. *bioRxiv* https://doi.org/10.1101/2020.10.27.357079.

21. Prasanna, X., V. T. Salo, …, E. Ikonen. 2020. Seipin traps triacylglycerols to facilitate their nanoscale clustering in the ER membrane. *bioRxiv* https://doi.org/10.1101/2020.10.26.355065.

22. Renvoisé, B., B. Malone, …, C. Blackstone. 2016. Reep1 null mice reveal a converging role for hereditary spastic paraplegia proteins in lipid droplet regulation. *Hum. Mol. Genet.* 25:5111–5125.

23. Zoni, V., R. Khaddaj, …, S. Vanni. 2020. Lipid droplet biogenesis is driven by liquid-liquid phase separation. *Dev. Cell*, Published online January 30, 2020.

24. Spanova, M., D. Zweytick, …, G. Daum. 2012. Influence of squalene on lipid particle/droplet and membrane organization in the yeast *Saccharomyces cerevisiae*. *Biochim. Biophys. Acta*. 1821:647–653.

25. Petranyi, G., N. S. Ryder, and A. Stütz. 1984. Allylamine derivatives: new class of synthetic antifungal agents inhibiting fungal squalene epoxidase. *Science*. 224:1239–1241.

26. Brown, A. J., N. K. Chua, and N. Yan. 2019. The shape of human squalene epoxidase expands the arsenal against cancer. *Nat. Commun.* 10:888.

27. Cirmena, G., P. Franceschelli, …, G. Zoppoli. 2018. Squalene epoxidase as a promising metabolic target in cancer treatment. *Cancer Lett.* 425:13–20.

28. Chorlay, A., and A. R. Thiam. 2018. An asymmetry in monolayer tension regulates lipid droplet budding direction. *Biophys. J.* 114:631–640.

29. Chorlay, A., L. Monticelli, …, A. Rachid Thiam. 2019. Membrane asymmetry imposes directionality on lipid droplet emergence from the ER. *Dev. Cell.* 50:25–42.e7.

30. Pautot, S., B. J. Frisken, and D. A. Weitz. 2003. Production of unilamellar vesicles using an inverted emulsion. *Langmuir.* 19:2870–2879.

31. Hochmuth, R. M., and E. A. Evans. 1982. Extensional flow of erythrocyte membrane from cell body to elastic tether. I. Analysis. *Biophys. J.* 39:71–81.

32. Olbrich, K., W. Rawicz, …, E. Evans. 2000. Water permeability and mechanical strength of polyunsaturated lipid bilayers. *Biophys. J.* 79:321–327.

33. Chabanon, M., J. C. S. Ho, …, P. Rangamani. 2017. Pulsatile lipid vesicles under osmotic stress. *Biophys. J.* 112:1682–1691.

34. Oglęcka, K., P. Rangamani, …, A. N. Parikh. 2014. Oscillatory phase separation in giant lipid vesicles induced by transmembrane osmotic differentials. *eLife.* 3:e03695.

35. Sandre, O., L. Moreaux, and F. Brochard-Wyart. 1999. Dynamics of transient pores in stretched vesicles. *Proc. Natl. Acad. Sci. USA.* 96:10591–10596.

36. Karatekin, E., O. Sandre, …, F. Brochard-Wyart. 2003. Cascades of transient pores in giant vesicles: line tension and transport. *Biophys. J.* 84:1734–1749.

37. Chorlay, A., A. Santinho, and A. R. Thiam. 2020. Making droplet-embedded vesicles to model cellular lipid droplets. *STAR Protoc.* 1:100116.

38. Faugeras, V., O. Duclos, …, A. R. Thiam. 2020. Membrane determinants for the passive translocation of analytes through droplet interface bilayers. *Soft Matter.* 16:5970–5980.

39. Needham, D., and D. A. Haydon. 1983. Tensions and free energies of formation of "solventless" lipid bilayers. Measurement of high contact angles. *Biophys. J.* 41:251–257.

40. Evans, E., V. Heinrich, …, W. Rawicz. 2003. Dynamic tension spectroscopy and strength of biomembranes. *Biophys. J.* 85:2342–2350.

41. Kwok, R., and E. Evans. 1981. Thermoelasticity of large lecithin bilayer vesicles. *Biophys. J.* 35:637–652.

42. Rawicz, W., K. C. Olbrich, …, E. Evans. 2000. Effect of chain length and unsaturation on elasticity of lipid bilayers. *Biophys. J.* 79:328–339.

43. Pakkanen, K. I., L. Duelund, …, J. H. Ipsen. 2011. Mechanics and dynamics of triglyceride-phospholipid model membranes: implications for cellular properties and function. *Biochim. Biophys. Acta.* 1808:1947–1956.

44. Hamilton, J. A. 1989. Interactions of triglycerides with phospholipids: incorporation into the bilayer structure and formation of emulsions. *Biochemistry.* 28:2514–2520.

45. Pakkanen, K. I., L. Duelund, …, J. H. Ipsen. 2010. Phase coexistence in a triolein-phosphatidylcholine system. Implications for lysosomal membrane properties. *Chem. Phys. Lipids.* 163:218–227.

46. Bacle, A., R. Gautier, …, S. Vanni. 2017. Interdigitation between triglycerides and lipids modulates surface properties of lipid droplets. *Biophys. J.* 112:1417–1430.

47. Tarun, O. B., M. Y. Eremchev, and S. Roke. 2018. Interaction of oil and lipids in freestanding lipid bilayer membranes studied with label-free high-throughput wide-field second-harmonic microscopy. *Langmuir.* 34:11305–11310.

48. Hildebrandt, E., A. Dessy, …, G. Leneweit. 2016. Interactions between phospholipids and organic phases: insights into lipoproteins and nano-emulsions. *Langmuir.* 32:5821–5829.

49. Bermúdez, H., D. A. Hammer, and D. E. Discher. 2004. Effect of bilayer thickness on membrane bending rigidity. *Langmuir.* 20:540–543.

50. Gross, L. C., A. J. Heron, …, M. I. Wallace. 2011. Determining membrane capacitance by dynamic control of droplet interface bilayer area. *Langmuir.* 27:14335–14342.

51. Waldbillig, R. C., and G. Szabo. 1979. Planar bilayer membranes from pure lipids. *Biochim. Biophys. Acta.* 557:295–305.

Supplemental Information

Fat inclusions strongly alter membrane mechanics

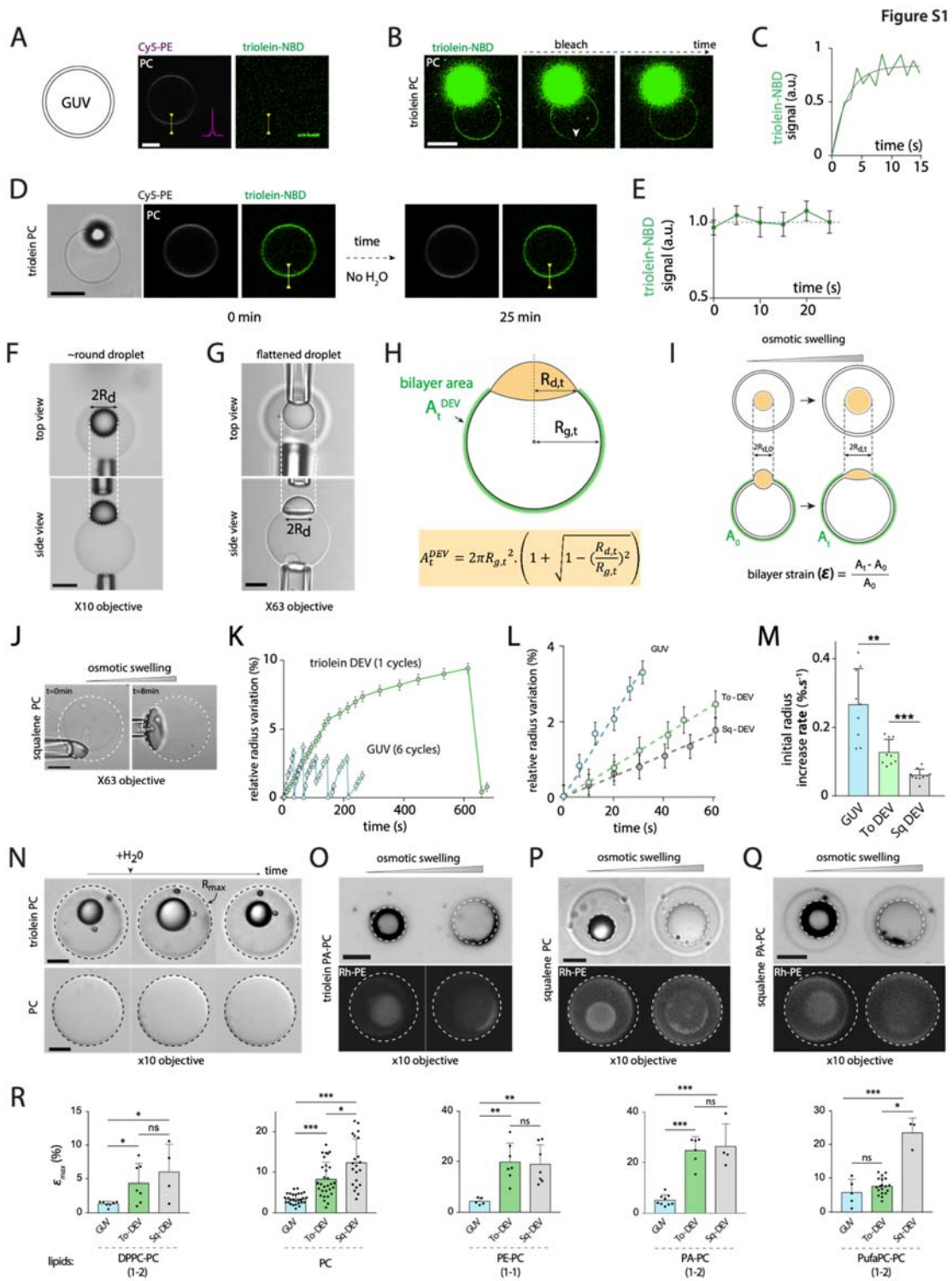Alexandre Santinho, Aymeric Chorlay, Lionel Foret, and Abdou Rachid Thiam

Supplemental figures

Figure S1

$$A_t^{DEV} = 2\pi R_{g,t}^2 \cdot \left(1 + \sqrt{1 - \left(\frac{R_{d,t}}{R_{g,t}}\right)^2}\right)$$

bilayer strain $(\varepsilon) = \dfrac{A_t - A_0}{A_0}$

Figure S1: related to figure 1

A) Confocal images of a PC GUV marked with Cy5-PE. The same settings as in Figure 2B were used for the green channel. No signal of triolein-NBD was visible here. Scale bar: 5µm. **B)** Confocal images of PC DEVs of triolein supplemented with 0,05% (w/w) triolein-NBD to report for triolein distribution. Image sequence of a FRAP (Fluorescence Recovery After Photobleaching) experiment on the bilayer. After bleaching the bilayer (see arrowhead), the triolein-NBD signal recovered. The scale bar is 5µm. **C)** Over time quantification of normalized triolein-NBD fluorescence signal after bleaching showing recovery. The non-linear fit matches the FRAP recovery curve. The fit was done with an exponential "one-phase association model". **D)** Confocal images of PC DEVs of triolein supplemented with triolein-NBD. The triolein DEVs were imaged for 25 minutes with no osmotic shock. The scale bar is 10µm. **E)** Over time variations of the triolein NBD-signal in the bilayer shows no variation of triolein concentration during 25 minutes. Absolute value +/- measurement uncertainty. **F)** Confocal bright field images captured at x10 objective of single PC DEV of triolein at a low tension state. Top view and side view showing the same droplet radius (R_d) used to compute the initial bilayer area of a DEV. The scale bar is 10µm. **G)** Confocal bright field images captured at x63 objective of single PC DEV of triolein at a high tension state with a flattened droplet. Top view and side view showing the same droplet radius (R_d) used to compute the final bilayer area of a DEV. The scale bar is 5µm. **H) Top:** Illustration of a DEV and needed parameters to compute the DEV bilayer area subtracting the area occupied by the embedded droplet. **Bottom:** Equation used to compute the bilayer area of a DEV. **I) Top:** Schematic representation of the bilayer area variations during osmotic swelling of a DEV (top view and side view). Green arcs underly the bilayer area. **Bottom:** Equation used to compute the bilayer strain ε. **J)** Representative images of a PC squalene-DEV observed at x63 objective during a hypotonic shock experiment. The first image corresponds to the unswollen state and the second to one of the critical bilayer strain before burst. Dashed circles report maximum radius. Scale bar: 10µm. **K)** Related to Figure 1B. The plot of the relative vesicle radius variations of triolein DEV and GUV over time. Swelling and burst cycles are visible for GUVs (blue points; 6 cycles) and DEVs (green points; 1 cycle). Absolute value +/- measurement uncertainty. **L)** Plot of the vesicle relative radius variation at the beginning of a swelling experiment of a GUV (blue points), a triolein DEV (green points), and a squalene DEV (grey points). The slope of the linear fit (dotted lines on the graph) was used to determine the initial radius increase rate. Absolute value +/- measurement uncertainty. **M)** Plot of the initial radius increase rate of PC bilayer of GUVs (n=8), triolein-DEVs (n=9), and squalene DEVs (n=9). Mean +/- SD. **N)** Time-lapse of triolein DEV and GUV during a

hypotonic shock experiment. Black dashed circles report maximum radius. The scale bar is 5μm. **O)** Representative images of a PC-PA triolein-DEV during a hypotonic shock experiment. The first image corresponds to the unswollen state and the second to the bilayer critical strain before burst. Dashed circles report maximum radius. Scale bar: 10μm. **P)** Representative images of a PC squalene-DEV during a hypotonic shock experiment. The first image corresponds to the unswollen state and the second to the bilayer critical strain before burst. Dashed circles report maximum radius. Scale bar: 10μm. **Q)** Representative images of a PC-PA squalene-DEV during a hypotonic shock experiment. The first image corresponds to the unswollen state and the second to the bilayer critical strain before burst. Dashed circles report maximum radius. Scale bar: 10μm. **R)** Detailed plots of figure 1F. Critical bilayer strain is shown for each phospholipids conditions with a student t-test. Stars indicate if means are significantly different or not. Mean +/- SD.
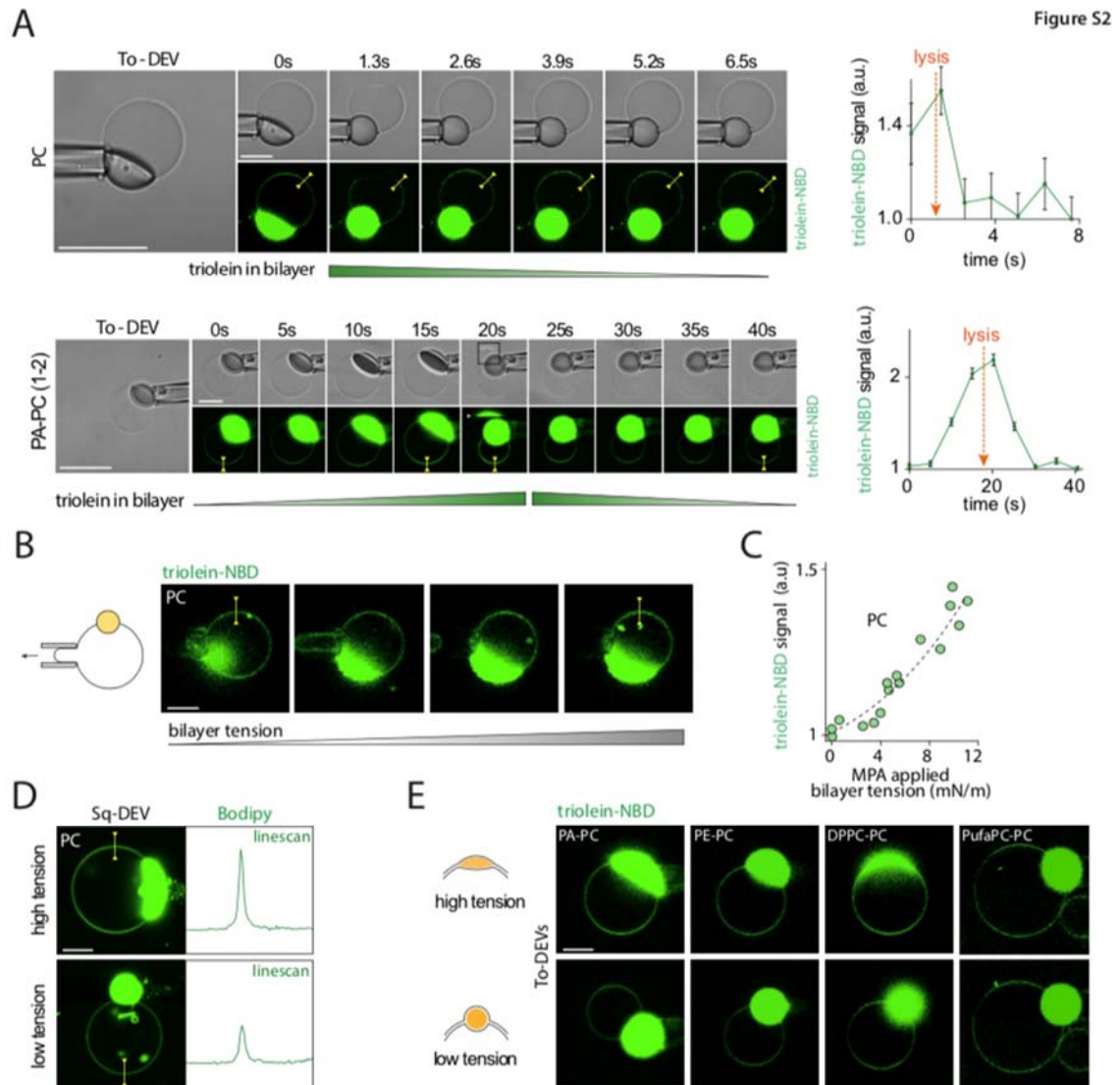
Figure S2: related to figure 2

A) Top: Time course of confocal images of a PC triolein-DEV (left) just after the burst of the vesicle. The scale bar is 20μm. Corresponding quantification of the amount of oil (right) in the bilayer shows a fast recovery of low triolein level after burst (few seconds). Absolute value +/- measurement uncertainty. **Bottom**: Time coarse of confocal images of a PC-PA triolein-DEV (left) before and after the burst. The scale bar is 20μm. Corresponding quantification of the amount of oil (right) in the bilayer shows a fast increase of oil level before burst followed by a rapid decrease of oil level after burst (few seconds). Absolute value +/- measurement uncertainty.

B) Left, Illustration of the method used to increase the bilayer tension of a triolein-DEV thanks to the micropipette aspiration technique. **Right**, the triolein-NBD signal in the bilayer of a PC triolein-DEVs during MPA-applied bilayer tension increase. Scale bar: 5μm. **C)** Plot of the triolein-NBD signal in bilayer against MPA-applied bilayer tension for PC triolein-DEVs. n=4 experiments. **D)** Confocal images of PC Sq-DEVs during the swelling experiment with bodipy, a hydrophobic probe. Scale bar: 5μm. A line scan of the bodipy signal in the bilayer is shown both in the stretched and unstretched state. **E)** Visualization of triolein-NBD signal in the bilayer during a hypotonic shock of PA-PC, PE-PC, DPPC-PC, and PufaPC-PC of triolein-DEVs both in the stretched and unstretched state. Scale bar: 5μm.
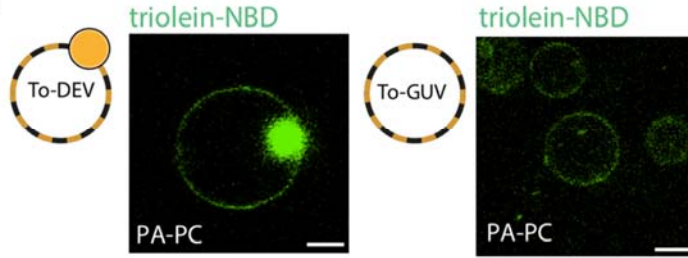
A

To-DEV

triolein-NBD

PA-PC

To-GUV

triolein-NBD

PA-PC

B

triolein in bilayer (a.u.)

ns

***

1.5

1

0.5

0
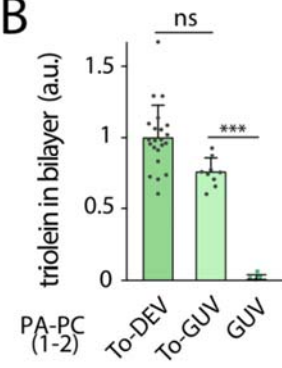
PA-PC
(1-2)

To-DEV   To-GUV   GUV

Figure S3: related to figure 3

A) Confocal images of PA-PC triolein-DEV and triolein-GUV with triolein-NBD. Scale bar: 5μm. **B)** Plot of the triolein in bilayer for PC-PA GUVs (n=4), triolein-GUVs (n=9), and triolein-DEVs (n=22). Mean +/- SD.

A

pore: bilayer lysis

pipette

bilayer

tension (γ)

B

lysis - tension (mN/m)

*

ns

ns

PA PC
(1:2)

GUV   To-DEV   Sq-DEV

C

triolein - NBD

γ

bilayer area

D

MPA-applied bilayer tension (mN/m)

GUV   To-GUV

Y_{app}

bilayer deformation (a.u.)

E

L_p L_t

bilayer nanotube

$2R_p$ R_g $2R_t$

Tube length (L_t)

Tongue length (L_p)

γ fixed

$$K = 2.\gamma.R_t^2$$

F

triolein - NBD

bilayer nanotube

G

L_p (μm)

δ

To - GUV

L_t (μm)

$R_t = -\delta.(1-R_p/R_g).R_p$

H

Nc hysteresis

L_p (μm)

To - GUV

L_t (μm)

$V_{pull} = 2.5 +/- 1$ μm.s^{-1}

I

No hysteresis

L_p (μm)

Sq - GUV

L_t (μm)
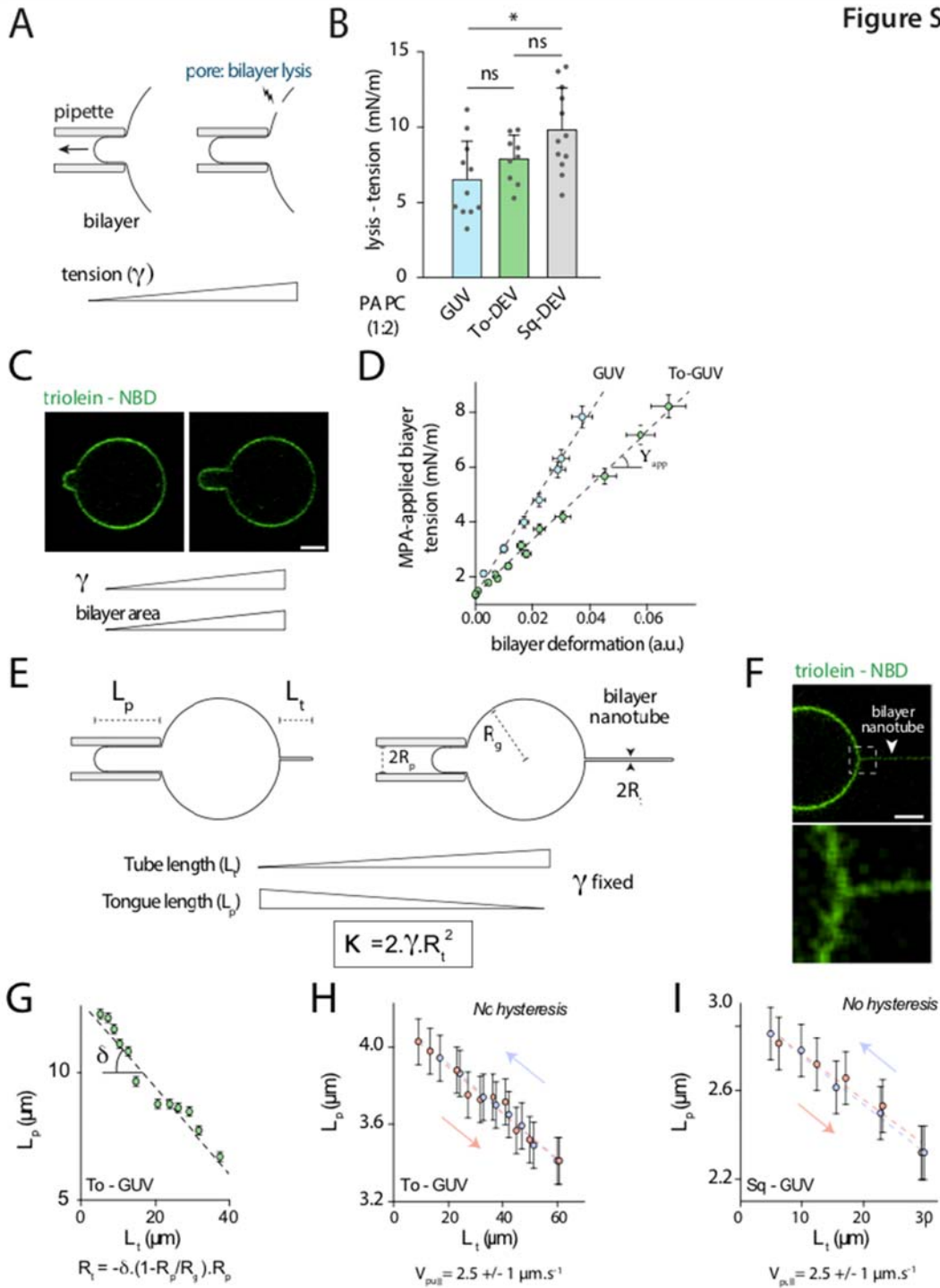
$V_{p,\parallel} = 2.5 +/- 1$ μm.s^{-1}

Figure S4: related to figure 4

A) Illustration of the method used for lysis tension determination. The bilayer tension of a vesicle is raised with a micropipette until the bilayer ruptures. Lysis tension is taken as the higher sustainable tension just before rupture. **B)** Membrane lysis tension of GUVs (n=11), triolein-DEVs (n=9) and squalene-DEVs (n=12) made with PC-PA. Mean +/- SD. **C)** Confocal images corresponding to the determination of the apparent area expansion modulus on a triolein-GUV with a triolein-NBD signal. Membrane tension is raised and the associated variation of the area is recorded. Scale bar: 5μm. **D)** Plot of the MPA-applied bilayer tension against area relative variation for a PC GUV (blue points) and a PC triolein-GUV (green points). Absolute value +/- measurement uncertainty. The slopes of the linear fits (dotted lines) are the elastic modulus of the corresponding GUV and triolein-GUV. **E)** Illustration of the determination protocol of the bending modulus computed with the membrane tension and the tube radius obtained by varying the tube length and recording the associated tongue length. **F)** Confocal images of a nanotube pulled from a PC triolein-DEV. Scale bar: 5μm. Zoom on the nanotube where a triolein-NBD signal is visible. Scale bar: 1μm. **G)** Example of a tongue length against tube length plot. The slope is linked with the nanotube radius which then allows computing the bending modulus. **H)** Tongue length against tube length plot for a triolein-GUV. The nanotube is pulled (red points) from the triolein-GUV and pushed (blue points) towards the triolein-GUV at a constant velocity of 2.5 +/- 1μm/s. Absolute value +/- measurement uncertainty. No hysteresis was detected indicating that oil partitioning is at the equilibrium during the tube pulling experiment. **G)** Tongue length against tube length plot for a squalene-GUV. The nanotube is pulled (red points) from the squalene-GUV and pushed (blue points) towards the squalene-GUV at a constant velocity of 2.5 +/- 1μm/s. Absolute value +/- measurement uncertainty. No hysteresis was detected indicating that oil partitioning is at equilibrium during the experiment.

Supplemental Text.

Supplementary materials: initial permeability determination for GUVs and DEVs

A. Fick law: conditions of utilization

Diffusion times of solutes through a phospholipid bilayer are negligible compared to the diffusion time of water. We therefore considered the diffusion of solutes through the bilayer of GUVs (or DEVs) as negligible compared to the diffusion of water. In this condition, Fick law leads to:

$$\frac{dV_t}{dt} = -\boldsymbol{P}.S_t.v_m.\Delta C(t)$$

where V_t is the volume inside the vesicle delimitated by S_t the area of permeation (ie area of bilayer), P the bilayer permeability to water, v_m the molar volume of water (18g.mol^{-1}) and $\Delta C(t)$ the difference of solutes concentration between the outside $C^e(t)$ and the inside $C^i(t)$ of the vesicle.

$$\Delta C(t) = C^e(t) - C^i(t)$$

B. $\Delta C(t)$: hypothesis and computation as a function of $R_{g,t}$

In our experiments, we considered only the first cycle of swelling and the first minute of experiment because it is difficult to characterize the concentration of solutes inside a GUV or a DEV after the first burst. We assume the concentration of solutes in the buffer to be constant and equal to the initial outside concentration C_0^e (145mOsm) as the buffer volume (220μL) is far greater than the volume of the vesicles having a radius between 5μm and 15μm (between 1pL and 15pL in volume). The concentration in the vesicle is equal to the initial one adjusted by the dilution factor $\frac{V_0}{V_t}$ where V$_0$ is the initial volume of the vesicle.

$$\Delta C(t) = C_0^e - C_0^i.\frac{V_0}{V_t} = C_0^i.(\frac{C_0^e}{C_0^i} - \frac{R_{g,0}^3}{R_{g,t}^3})$$

Where R$_{g,t}$ and R$_{g,0}$ are respectively the vesicle radius at the time t and at the beginning of swelling (**Figure 1**). As we have small variations of radius (<10%). We made the approximation that:

$$R_{g,t} = \delta R_{g,t} + R_{g,0}$$

where $\delta R_{g,t}$ represent the small variations of vesicle radius.

It follows that:

$$\Delta C(t) = C_0^i \cdot \left(\frac{C_0^e}{C_0^i} - \frac{1}{(1 + \frac{\delta R_{g,t}}{R_{g,0}})^3} \right)$$

At the first order we have:

$$\Delta C(t) = C_0^i \cdot \left(\frac{C_0^e}{C_0^i} + \left(3 \frac{\delta R_{g,t}}{R_{g,0}} - 1 \right) \right)$$

Then we have:

$$\Delta C(t) = C_0^i \cdot \left(\frac{C_0^e}{C_0^i} + 3 \frac{R_{g,t}}{R_{g,0}} - 4 \right)$$

Now that $\Delta C(t)$ is determine, in next, C&D, we will determine the exact surface and volume of DEV involve in the Fick law.

C. GUV and DEV permeation surface: hypothesis and computation as a function of $R_{g,t}$

The permeation surface of the GUV (S_t^{GUV}) corresponds to the surface of the sphere formed by its bilayer and can be expressed as:

$$S_t^{GUV} = 4\pi R_{g,t}^2$$

In the case of the DEV, the water cannot pass through the oil droplet. Thus to assess the permeation surface of a DEV (S_t^{DEV}) we have to subtract the surface area occupied by the droplet S_t^{cap} from the surface area of the sphere forming its bilayer S_t^{GUV} (see **Figure 1**) :

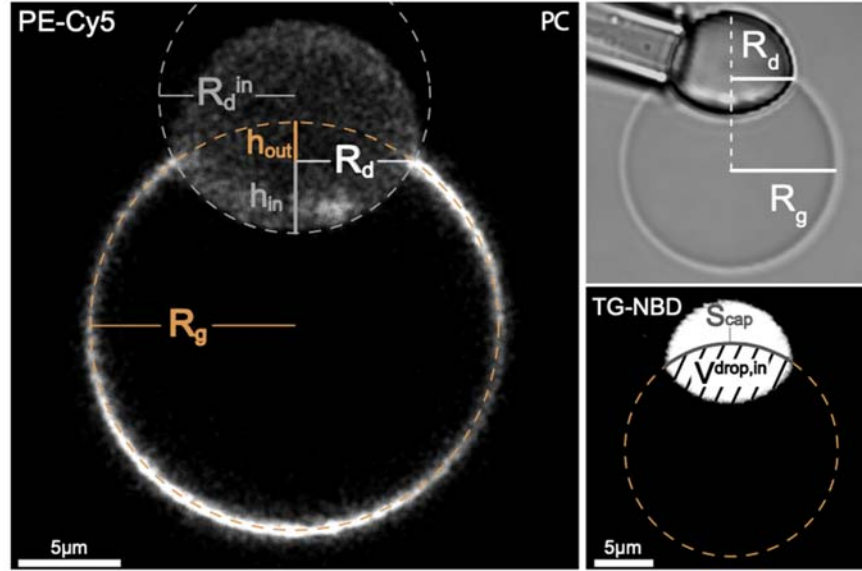$$S_t^{DEV} = S_t^{GUV} - S_t^{cap}$$

Figure 1: triolein-DEVs of DOPC at x63 objective showing parameters to compute the corrected surface and volume of a DEV.

Note that both S_t^{cap} and S_t^{GUV} (**Figure 1**) are varying over time due to the variations of the vesicle $R_{g,t}$ and the droplet radii $R_{d,t}$ (**Figure 2**).
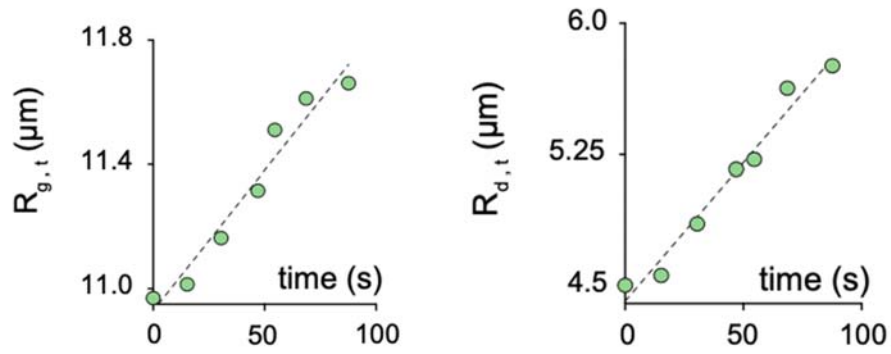

Figure 2: Plot of R_g and R_d as a function of time

S_t^{cap} can be calculated as follow:

$$S_t^{cap} = 2\pi R_{g,t}^2 \cdot \left(1 - \sqrt{1 - (\frac{R_{d,t}}{R_{g,t}})^2}\right)$$

Following, we have S_t^{DEV}:

$$S_t^{DEV} = 2\pi R_{g,t}^2 \cdot \left(1 + \sqrt{1 - (\frac{R_{d,t}}{R_{g,t}})^2}\right)$$

Compared to an equivalent droplet-free vesicle, the permeation area of the DEV must therefore be corrected by the following factor:

$$\beta_t = \frac{S_t^{DEV}}{S_t^{GUV}} = \frac{1}{2}\left(1 + \sqrt{1 - (\frac{R_{d,t}}{R_{g,t}})^2}\right)$$

Correction factor β_t:

As the radius of the vesicle ($R_{g,t}$) and the radius of the droplet ($R_{d,t}$) evolved during the osmotic swelling (**Figure 2**), we calculated β_t over time and found that it only varied from 0,922 to 0,899. These variations are represented in **Figure 3**.
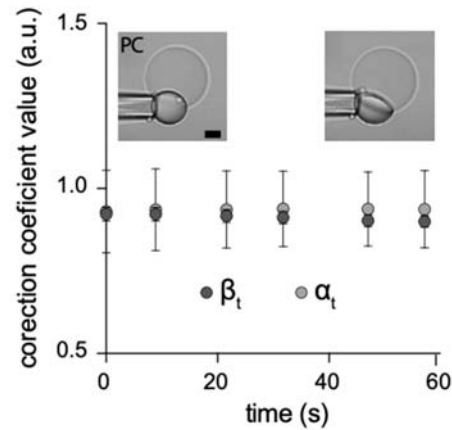

Figure 3: Plot of the correction coefficient α and β

In order to better quantify this small decrease of β_t , we calculated the ratio between the initial β_t and its value after 60 second of each osmotic swelling experiment (β_{60}/β_0, Figure 4, right). We find that β_t has very small variations: 2,15 $\pm$ 0.67 % and 1,04 $\pm$ 0.69 % respectively for To-DEV and Sq-DEV (**Figure 4, right**). Based on these observations, we considered $\beta_t = \beta_0$. We plotted all the value of β_0 in (**Figure 4, left**).
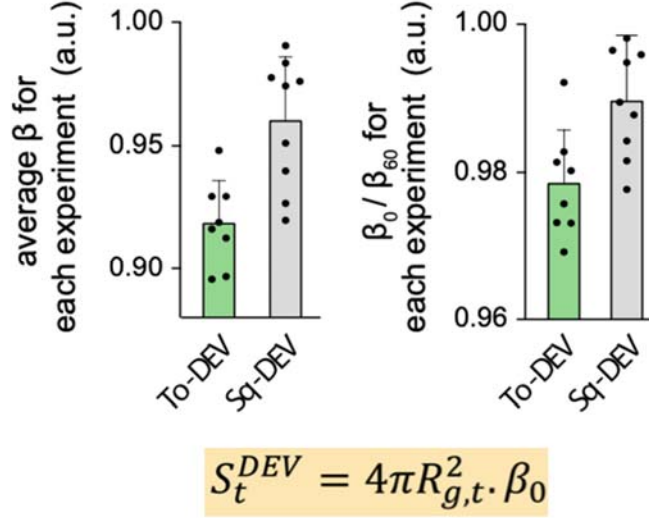
$$S_t^{DEV} = 4\pi R_{g,t}^2 \cdot \beta_0$$

Figure 4: Left: Mean value of β for DEVs permeability assay; Right: Variations of β during permeability experiment.

We thus have a surface of permeation S_t which can written as:

$$S_t = \beta_0 . 4\pi R_{g,t}{}^2 \text{ for DEV and } S_t = 4\pi R_{g,t}{}^2 \text{ for GUVs}$$

D. GUV and DEV volume: hypothesis and computation as a function of $R_{g,t}$

For the volume of a GUV, V_t can be expressed as:

$$V_t^{GUV} = \frac{4}{3}\pi R_{g,t}{}^3$$

The inside DEV volume V_t^{DEV} has to be corrected because of the presence to the droplet:

$$V_t^{DEV} = V_t^{GUV} - V_t^{drop,in}$$

where $V_t^{drop,in}$ is the lacking of aqueous volume in the vesicle occupied by the embedded droplet (see Figure S1A). V_t^{DEV} can be expressed as:

$$V_t^{DEV} = \frac{4}{3}\pi R_{g,t}{}^3 - \frac{\pi}{3}\left(h_{out,t}^2\left(3R_{g,t} - h_{out,t}\right) + \left(h_{in,t}^2\left(3R_{drop,t}^{in} - h_{in,t}\right)\right)\right.$$

where $h_{out,t}$, $h_{in,t}$ and $R_{drop,t}^{in}$ are all defined in **Figure 1**.

It follows:

$$\frac{V_t^{DEV}}{V_t^{GUV}} = 1 - \frac{\left(h_{out,t}^2\left(3R_{g,t} - h_{out,t}\right) + \left(h_{in,t}^2\left(3r_{drop,t}^{in} - h_{in},t\right)\right)\right.}{4R_{g,t}^3} = \alpha_t$$

For the experiment in **figure 2** the variation of α_t are plotted as a function of time (**Figure 3**).

Correction factor α_t:

Where α_t is the correction factor of the DEV inner volume compared to the one of GUVs. As we did previously for β_t , α_t is plotted as a function of time (Figure 3). The variation of α_t is also very small, from 0,930 to 0,937. We also examined for each experiment the variations of α_t during the first 60 seconds α_{60}/α_0 (Figure 5, right) which were very small: $1{,}11 \pm 0.35\,\%$ and $0{,}50 \pm 0.48\,\%$ respectively for To-DEV and Sq-DEV (**Figure 5, right**). Based on these observations, we considered $\alpha_t = \alpha_0$. We plotted all the value of α_0 in (**Figure 5 left**).
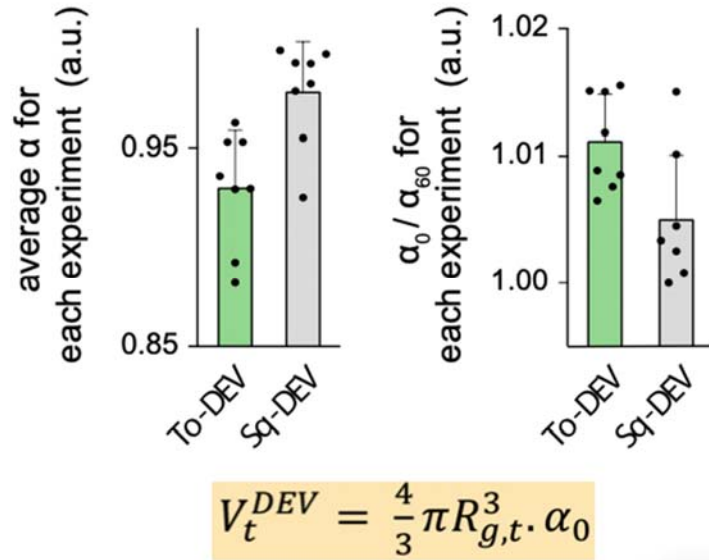

$$V_t^{DEV} = \frac{4}{3}\pi R_{g,t}^3 \cdot \alpha_0$$

Figure 5: Left: Mean value of α for DEVs permeability assay; Right: Variations of α during permeability experiment.

In conclusion, the volume of permeation of a DEV and a GUV write as:

$$V_t = \alpha_0 . \frac{4}{3}\pi R_{g,t}{}^3 \quad \text{for DEVs and} \quad V_t = \frac{4}{3}\pi R_{g,t}{}^3 \quad \text{for GUVs}$$

E. Fick law with $R_{g,t}$ as the sole variable:

Considering the expression $\Delta C(t)$ established in B. one obtains:

$$\frac{dV_t}{dt} = -P.S_t.v_m.C_0^i.\left(\frac{C_0^e}{C_0^i} + 3\frac{R_{g,t}}{R_{g,0}} - 4\right)$$

Replacing V_t and S_t by their expression obtained in C. and D leads to:

$$\frac{d(\alpha_0 . \frac{4}{3}\pi R_{g,t}{}^3)}{dt} = -P.\beta_0.4\pi R_{g,t}{}^2.v_m.C_0^i.\left(\frac{C_0^e}{C_0^i} + 3\frac{R_{g,t}}{R_{g,0}} - 4\right)$$

We obtain a differential equation of the first order with a constant second member:

$$\frac{d(\frac{R_{g,t}}{R_{g,0}})}{dt} + \frac{3P.\beta_0.\alpha_0^{-1}.v_m.C_0^i}{R_{g,0}}\frac{R_{g,t}}{R_{g,0}} = \frac{P.\beta_0.\alpha_0^{-1}.v_m.C_0^i}{R_{g,0}}.\left(4 - \frac{C_0^e}{C_0^i}\right)$$

So:

$$\frac{d\left(\frac{R_{g,t}}{R_{g,0}}\right)}{dt} + a\frac{R_{g,t}}{R_{g,0}} = \frac{a}{3}\left(4 - \frac{C_0^e}{C_0^i}\right) \quad \text{where} \quad a = \frac{3P.\beta_0.\alpha_0^{-1}.v_m.C_0^i}{R_{g,0}}$$

As we have linear curve for $\frac{R_{g,t}}{R_{g,0}}$ for the first 60 seconds (**Figure S1L**), $\frac{d\left(\frac{R_{g,t}}{R_{g,0}}\right)}{dt} = \omega$ is constant

and equal to the slope of $\frac{R_{g,t}}{R_{g,0}}$.

$$\omega = \left(\left(4 - \frac{C_0^e}{C_0^i}\right) - 3\frac{<R_{g,t}>}{R_{g,0}}\right)\frac{P_{initial}.\beta_0.\alpha_0^{-1}.v_m.C_0^i}{R_{g,0}}$$

Here, $P_{initial}$, "initial permeability" replaces the permeability because we considered only initial slope at the beginning of experiment. For a given experiment, $<R_{g,t}>$ is the mean of $R_{g,t}$ in the first 60 seconds.

$$P_{initial} = \frac{\omega.R_{g,0}}{\beta_0.\alpha_0^{-1}.v_m.((4-3\frac{<R_{g,t}>}{R_{g,0}})C_0^i-C_0^e)}$$

With this expression, we determined the initial permeability to water $P_{initial}$ for PC GUVs, PC triolein-DEVs and PC squalene-DEVs. (**Principal Figure 1E, left**)